

Isometric Motion Manifold Primitives

Yonghyeon Lee¹

Abstract—The Motion Manifold Primitive (MMP) produces, for a given task, a continuous manifold of trajectories each of which can successfully complete the task. It consists of the decoder function that parametrizes the manifold and the probability density in the latent coordinate space. In this paper, we first show that the MMP performance can significantly degrade due to the geometric distortion in the latent space – by distortion, we mean that similar motions are not located nearby in the latent space. We then propose *Isometric Motion Manifold Primitives* (IMMP) whose latent coordinate space preserves the geometry of the manifold. For this purpose, we formulate and use a Riemannian metric for the motion space (i.e., parametric curve space), which we call a *CurveGeom Riemannian metric*. Experiments with planar obstacle-avoiding motions and pushing manipulation tasks show that IMMP significantly outperforms existing MMP methods. Code is available at <https://github.com/Gabe-YHLee/IMMP-public>.

Index Terms—Movement Primitives, Manifold, Isometric Representation Learning, Autoencoders, Riemannian Geometry

I. INTRODUCTION

The *Motion Manifold Primitives (MMP)* framework provides a highly adaptable primitive model, that encodes and generates, for a given task, a continuous manifold of trajectories each of which is capable of accomplishing the task [1], [2]. For example, consider an example shown in Fig. 1, where six different demonstration trajectories of a 2D mobile robot are given (red and blue trajectories). These trajectories – which are originally viewed as elements of the infinite-dimensional trajectory space (or, given discrete representations, finite but very high-dimensional trajectory space) – can be assumed to be approximately lying on some reasonably lower-dimensional manifold. In the machine learning context, this assumption is called the manifold hypothesis and has been widely accepted as one of the fundamental principles for studying high-dimensional datasets [3]–[5].

Representing basic motion skills using motion manifold primitives offers a much higher level of adaptability compared to many existing movement primitives that encode only a single trajectory for a given task such as the dynamic movement primitives [6]–[11], stable dynamical systems [12]–[17], methods based on Gaussian processes [18], [19] and Gaussian mixture models [20]–[22], and other methods [23]–[25]. Specifically, even when certain trajectories become infeasible in new environments (e.g., blocked by unseen obstacles), the motion manifold primitives can generate alternative feasible trajectories, unlike single trajectory-based movement primitives. This enhanced adaptability stems from a more diverse range of demonstration data experienced in training.

¹Center for AI and Natural Sciences (CAINS), Korea Institute for Advanced Study (KIAS), Seoul, South Korea, ylee@kias.re.kr

This work has been submitted to the IEEE for possible publication. Copyright may be transferred without notice, after which this version may no longer be accessible.

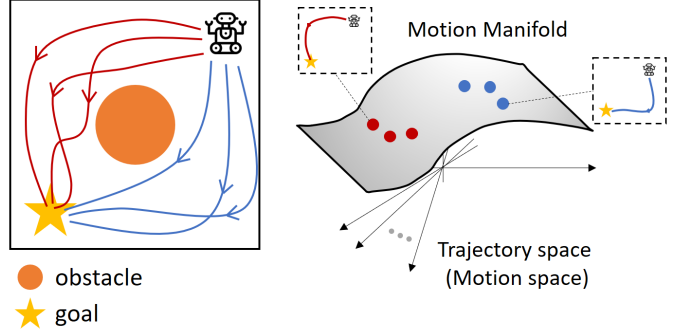


Fig. 1. A set of multiple trajectories does not occupy the entire trajectory space – which is infinite-dimensional – but lies approximately on some finite lower-dimensional non-linear subspace or manifold, which is called the Motion Manifold.

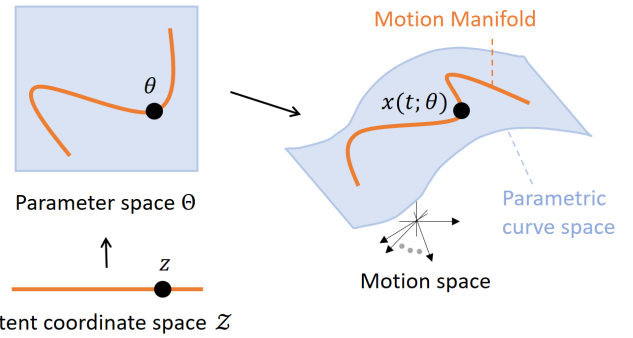


Fig. 2. A latent coordinate space \mathcal{Z} is mapped to a subspace of the finite-dimensional parameter space Θ ; the parameter space Θ is mapped to a subspace of the infinite-dimensional motion space. Consequently, the latent space \mathcal{Z} is mapped to a subspace of the motion space, which we consider as a motion manifold. The motion manifold and parametric curve space are visualized as a curve and surface, not because their actual dimensions are one and two, but only to indicate the relative size relationships of their dimensions.

To learn motion manifold primitives, the first step would be to select numerical representations of motions. In recent methods [1], [2], motions are represented as fixed-length discrete-time trajectories, e.g., a motion is a sequence of configurations (x_1, x_2, \dots, x_T) for a positive integer T . Instead, in this work, we represent motions with *parametric curve models* $x(t; \theta)$ for $t \in [0, T]$ (e.g., Bezier curve [26]), which have several advantages. First, motions have bounded accelerations and jerks, avoiding sudden and abrupt changes. Second, the dimension of the parametric curve space, i.e., the dimension of $\{x(t; \theta) \mid \theta \in \Theta\}$, is in general much smaller than the dimension of the discrete-time trajectory data space, reducing the difficulty of the following manifold primitive learning problem. For the above reasons, we represent motions with parametric curves.

The problem of learning motion manifold primitives can

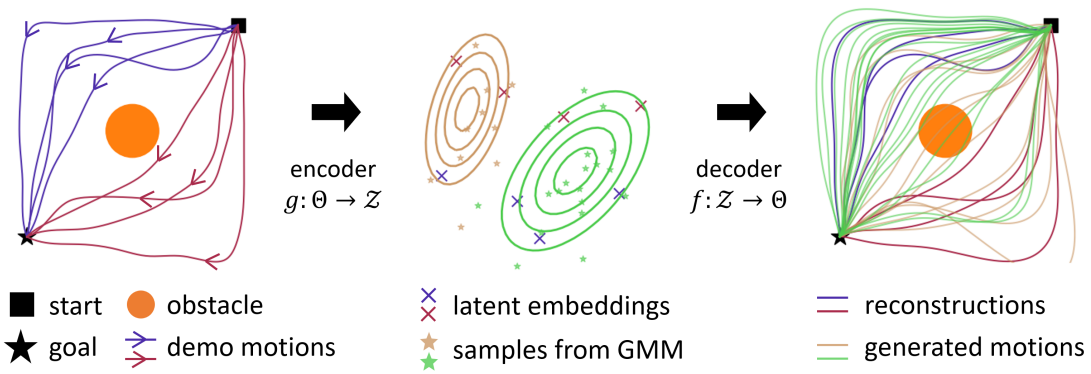


Fig. 3. *Left*: There are eight demonstration motions (red and blue trajectories) that travel from the start to the goal, avoiding the obstacle, where each motion is represented with a Bezier curve parameter θ (i.e., positions of the control points); for this example, it consists of 10 control points and thus is 20-dimensional. *Middle*: The encoder trained with a two-dimensional latent space maps the demo motions $\{\theta_i\}_{i=1}^8$ to the latent embeddings $\{z_i\}_{i=1}^8$; a Gaussian Mixture Model (GMM) of two components is trained with $\{z_i\}$ (light brown and green concentric ellipses); sample latent points from the GMM are visualized as light brown and green stars. *Right*: The trained decoder reconstructs the latent embeddings $\{z_i\}$ to the original demo trajectories $\{\theta_i\}$; new motions, which are indicated by the light brown and green trajectories, are generated by decoding the sampled latent points.

then be formulated in the curve parameter space Θ . As shown in Fig. 2, our goal is to find a latent coordinate space $z \in \mathcal{Z}$ and a mapping f that maps $z \in \mathcal{Z}$ to $\theta \in \Theta$ which consequently maps to $x(t; \theta)$ in the motion manifold. In other words, the latent space \mathcal{Z} is mapped to a subspace of Θ via f and consequently mapped to the motion manifold embedded in the ambient motion space. An *autoencoder* method provides an appealing framework for simultaneously learning the latent coordinate space \mathcal{Z} and non-linear mapping $f : \mathcal{Z} \rightarrow \Theta$ that explicitly parametrizes the manifold [5], [27]–[31], where recent works in MMP have also adopted this approach [1], [2]. In this framework, the primary goal is to find a pair of mappings, an encoder $g : \Theta \rightarrow \mathcal{Z}$ and a decoder $f : \mathcal{Z} \rightarrow \Theta$ often approximated with deep neural networks, so that the composition $f \circ g$ reconstructs all the given data points. Then, given a suitable sampler in \mathcal{Z} (e.g., a probability density model), the decoder can generate curve parameters θ and the corresponding motions $x(t; \theta)$ for the task.

However, a naive application of the vanilla autoencoder method in the curve parameter space Θ often results in a *geometrically distorted* latent coordinate space – where similar motion data are not positioned close to each other –, leading to a generation of motions that violate the task constraint. For example, consider an example shown in Fig. 3, where we train an autoencoder with 8 demonstration trajectories represented by the corresponding Bezier curve parameters $\{\theta_i\}_{i=1}^8$ (we use 10 control points; thus $\Theta = \mathbb{R}^{20}$), using a two-dimensional latent space $\mathcal{Z} = \mathbb{R}^2$. We then fit a Gaussian Mixture Model (GMM) of two components in the latent space and generate latent samples and motions. As illustrated in Fig. 3 (*Middle*), due to the geometric distortion in the latent space, the same color trajectories are not located close enough to each other when compared to the other color trajectories. Consequently, the red and blue latent points are not correctly clustered by the GMM model, and many of the generated motions collide with the obstacle, failing to accomplish the task.

In this paper, adopting the isometric regularization method from [29], we propose to learn a *geometry-preserving mapping*

$f : \mathcal{Z} \rightarrow \Theta$ called a *scaled isometry*, so that similar trajectories can be located nearby in the latent space. To employ this method in our context, we need to specify a *Riemannian metric* for the curve parameter space Θ that serves as the basis for determining the notion of closeness in Θ . As done in [29], we may choose the Euclidean metric, i.e., $ds^2 = d\theta^T d\theta$. However, as one would intuitively anticipate, the Euclidean metric fails to accurately represent the geometry of the motion space (see Fig. 6). Therefore, the isometric regularization falls short of the desired results.

We propose a *CurveGeom Riemannian metric* for the space Θ , that reflects the geometry of the motion space, given a curve model $x(t; \theta)$ that satisfies some mild regularity conditions. We then show that using linear curve models induces constant CurveGeom metrics, leading to simpler implementations of the isometric regularization. Together with a probability density model (e.g., GMM) fitted in the latent coordinate space, the decoder trained with the isometric regularization is referred to as the *Isometric Motion Manifold Primitives (IMMP)*. Moreover, adopting the IMMP framework, we propose a method to train a stochastic policy that outputs a latent GMM given a state, which we refer to as the *Isometric Motion Manifold Policy (IMM π)*.

Experiments involving planar obstacle-avoidance motions and pushing manipulation tasks demonstrate that IMMP and IMM π – which are trained by using CurveGeom Riemannian metric – outperform existing MMP and MM π methods by a significant margin.

II. RELATED WORKS

A. Manifold Learning and Latent Space Distortion

An autoencoder framework and its variants have received a lot of attention as effective methods to learn the manifold and its coordinate chart simultaneously, including but not limited to [27], [29], [30], [32]–[36]. Of particular relevance to our paper, a geometric perspective on autoencoders has been eloquently presented in [5]. In our paper, a significant aspect of concern is the presence of the geometric distortion within

the latent space of the autoencoder, as highlighted in [5], [29], [35], [37], [38]. A recent regularization method [29] has developed a method to find the one that minimizes the geometric distortion, i.e., preserves the geometry of the data manifold as much as possible. However, in our problem setting, a naive application of [29] with the Euclidean metric assumption on the curve parameter space Θ does not produce desirable results because Euclidean metric does not capture the geometry of the actual curve spaces. The key difference in our method compared to [29] is the development of a suitable Riemannian metric for the parametric curve space Θ .

B. Riemannian Geometry of Data

There is a growing interest in Riemannian data, where taking into account the Riemannian metric of the data manifold leads to more natural and superior performance. For example, the space of rigid body orientations can be represented as the special orthogonal group $\text{SO}(3)$ with the bi-invariant Riemannian metric [39] or as the unit quaternion Riemannian manifold S^3 [40]. The space of positive-definite matrices can be assigned either the affine-invariant Riemannian metric [41] or the log-Euclidean metric [42], which find applications in medical imaging [41], [42], inertial parameter identification [43], and more [44]. Moreover, the space of the Grassmann manifold can be endowed with the metric derived from the quotient structure [45], which has been used to define the extrinsic curvature of manifolds [31]. Meanwhile, information geometry provides a natural Riemannian metric for the space of probability density functions, adopting the Fisher information metric [46], [47]. As a practical application, the space of Gaussian distributions can be endowed with the natural metric, which finds use in fiber tracking in DTI images [48]. Recently, the space of point cloud data has been equipped with the info-Riemannian metric, where points in each point cloud are treated as samples from its underlying probability density function [28]. In this context, our work can be seen as introducing a new Riemannian data – a Riemannian metric for the space of parametric curves.

III. RIEMANNIAN GEOMETRY OF PARAMETRIC CURVES

We begin this section with the introduction of the notations used throughout. We denote a configuration space by $X = \mathbb{R}^n$ and consider a smooth curve $x : [0, T] \rightarrow X$ as a representation of a motion, where the velocity norm is defined as $\|x\| := \sqrt{\dot{x}^T \dot{x}}$. The space of all smooth curves is considered an infinite-dimensional function space \mathcal{X} with an inner product defined as follows: $\langle v, w \rangle := \frac{1}{T} \int_0^T v(t)^T w(t) dt$ for two square-integrable functions $v, w : [0, T] \rightarrow \mathbb{R}^n$ (i.e., \mathcal{X} is a Hilbert space).

Of particular relevance to this paper is a parametric curve $x(t; \theta)$ where $\theta \in \Theta$ denotes the parameter of the curve and Θ is a compact subspace of \mathbb{R}^D . Consider the set of all parametric curves $\mathcal{X}_\Theta := \{x(\cdot; \theta) \in \mathcal{X} \mid \theta \in \Theta\}$. This space is a D -dimensional differentiable manifold under some mild conditions:

Proposition 1. Suppose a curve $x(t; \theta)$ is smooth in both t and θ and $x(t; \cdot) : \Theta \rightarrow \mathcal{X}$ is injective, i.e., if $x(t; \theta_1) = x(t; \theta_2)$

for all $t \in [0, T]$, then $\theta_1 = \theta_2$. Let $\theta = (\theta^1, \dots, \theta^D)$ and $v = (v^1, \dots, v^D) \in \mathbb{R}^D$, if

$$\sum_{i=1}^D \frac{\partial x(t; \theta)}{\partial \theta^i} v^i = 0 \implies v = 0 \quad (1)$$

for all $\theta \in \Theta$, then \mathcal{X}_Θ is a D -dimensional differentiable manifold.

Proof. A differentiable mapping $x(t; \cdot) : \Theta \rightarrow \mathcal{X}$ is injective and immersion by (1) and Θ is compact; thus the mapping is an embedding (i.e., \mathcal{X}_Θ is an embedded manifold in \mathcal{X}). \square

Given the parametric curve space \mathcal{X}_Θ , which is embedded in \mathcal{X} , the inner product $\langle \cdot, \cdot \rangle$ in \mathcal{X} can be naturally projected into \mathcal{X}_Θ . This leads to – by treating Θ as a local coordinate space for \mathcal{X}_Θ – the definition of the Riemannian metric that captures the geometry of the motion space in the parameter space Θ , which we denote by $H(\theta) = (h_{ij}(\theta))$. Specifically, the square of the length of an infinitesimal displacement $d\theta \in \mathbb{R}^D$ is

$$\begin{aligned} ds^2 &= \sum_{i,j} h_{ij}(\theta) d\theta^i d\theta^j \\ &= \int_0^T \left\langle \sum_i \frac{\partial x(t; \theta)}{\partial \theta^i} d\theta^i, \sum_j \frac{\partial x(t; \theta)}{\partial \theta^j} d\theta^j \right\rangle dt \\ &= \sum_{i,j} \left(\int_0^T \frac{\partial x(t; \theta)^T}{\partial \theta^i} \frac{\partial x(t; \theta)}{\partial \theta^j} dt \right) d\theta^i d\theta^j. \end{aligned} \quad (2)$$

This leads to a formal definition of the Riemannian metric in the parametric curve space Θ :

Definition 1. Let $\frac{\partial x(t; \theta)}{\partial \theta}$ be an $n \times D$ matrix, then

$$H(\theta) = \int_0^T \frac{\partial x(t; \theta)^T}{\partial \theta} \frac{\partial x(t; \theta)}{\partial \theta} dt \quad (3)$$

is a $D \times D$ positive-definite matrix and called a **CurveGeom Riemannian metric**.

Proof. Because of (1), $v^T H(\theta) v > 0$ for all $v \neq 0 \in \mathbb{R}^D$. \square

In this paper, we will focus on a particular class of curve models, a linear curve model, that is expressed as follows:

$$x(t; \theta) = \sum_{j=1}^d \theta^{ij} B_j(t), \quad (4)$$

where $\theta = (\theta^{ij})_{i=1, \dots, n, j=1, \dots, d} \in \mathbb{R}^{n \times d}$ – in which we use matrix representations of the curve parameters for convenience – and $B(t) = (B_1(t), \dots, B_d(t)) \in \mathbb{R}^d$. This model satisfies the condition in Proposition 1 and $\{\theta B(t) \mid \theta \in \Theta \subset \mathbb{R}^{n \times d}\}$ is an $n \times d$ -dimensional differentiable manifold, if $B_1(t), \dots, B_d(t)$ are linearly independent:

Proposition 2. Suppose $B_1(t), \dots, B_d(t)$ are linearly independent, i.e., if $a_1 B_1(t) + a_2 B_2(t) + \dots + a_d B_d(t) = 0$ for all $t \in [0, T]$, then $(a_1, \dots, a_d) = 0$. Then, the linear curve model (4) satisfies the injective immersion condition in Proposition 1.

Proof. Suppose $\theta_1 B(t) = \theta_2 B(t)$ for all t , which implies that $(\theta_1 - \theta_2) B(t) = \sum_{j=1}^d (\theta_1 - \theta_2)^{ij} B_j(t) = 0$ for all t and i . By the linearity, $\theta_1 = \theta_2$; the injectivity is proved. Now, suppose

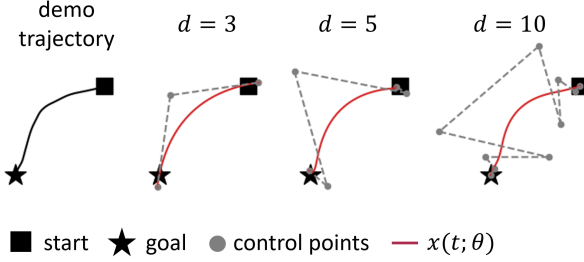


Fig. 4. A two-dimensional demonstration trajectory and Bezier curves fitting results with $d = 3, 5, 10$.

$\sum_{i,j} \frac{\partial x(t; \theta)}{\partial \theta^{ij}} v^{ij} = 0$, which implies that $\sum_j v^{ij} B_j(t) = 0$ for all t and i . Similarly, by the linearity, $v = 0$; thus the mapping $\theta \mapsto \theta B(t)$ is an immersion. \square

Given a linear curve model $x(t; \theta) = \theta B(t)$ for $\theta = (\theta^{ij}) \in \mathbb{R}^{n \times d}$ and $B(t) = (B_i(t)) \in \mathbb{R}^d$, the CurveGeom metric in (1) is constant and has the following representation:

$$h_{ijkl} = \delta_{ik} \int_0^T B_j(t) B_l(t) dt \quad (5)$$

for $i, k = 1, \dots, n$ and $j, l = 1, \dots, d$, where δ_{ik} is the Kronecker delta. We first note that the metric h_{ijkl} does not depend on θ . This is particularly useful for our later isometric motion manifold primitives learning, because we only need to compute the metric once before training. Given an infinitesimal displacement $d\theta \in \mathbb{R}^{n \times d}$, the square of the length is

$$ds^2 = \int_0^T \text{Tr}(B(t) B(t)^T d\theta^T d\theta) dt. \quad (6)$$

An additional advantage of using linear curve models is that, given a demonstration trajectory $\{(t_1, x_1), \dots, (t_N, x_N)\}$, fitting a linear curve $x(t; \theta)$ to the data can be formulated as a simple linear least square problem $\min_{\theta} \sum_{i=1}^N \|x(t_i; \theta) - x_i\|^2$; assuming $N > d$, there is a closed-form solution:

$$\theta = \mathbf{X} \mathbf{B}^T (\mathbf{B} \mathbf{B}^T)^{-1}, \quad (7)$$

where the data matrix $\mathbf{X} = (x_1, x_2, \dots, x_N) \in \mathbb{R}^{n \times N}$ and basis matrix $\mathbf{B} = (B(t_1), B(t_2), \dots, B(t_N)) \in \mathbb{R}^{d \times N}$.

A. Example: Bezier curves

In this section, we provide a concrete example of linear curve models, a Bezier curve [26], and its CurveGeom Riemannian metric. A Bezier curve of degree $d-1$ has the following explicit form: for $t \in [0, T]$ and $i = 1, \dots, n$,

$$\begin{aligned} x^i(t; \theta) &= \sum_{j=1}^d \theta^{ij} B_j(t) \\ &= \sum_{j=1}^d \theta^{ij} \binom{d-1}{j-1} \left(1 - \frac{t}{T}\right)^{d-j} \left(\frac{t}{T}\right)^{j-1}, \end{aligned} \quad (8)$$

where $\theta^{i1}, \dots, \theta^{id}$ are the control points for the i -th coordinate value x^i ; examples of Bezier curves fitted to a given demonstration data are shown in Fig. 4

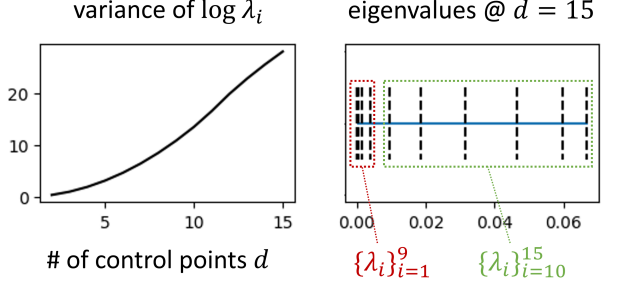


Fig. 5. Left: The variance of log eigenvalues as a function of d . Right: The distribution of eigenvalues of \bar{H} at $d = 15$.

We compute the CurveGeom metric (5) via a numerical integration over t . One may think it is a computation-heavy process, but fortunately, since it is constant over θ , we only need to compute it once. In the remaining section, we will discuss how much the CurveGeom metric can differ from the (scaled) identity metric as the number of control points d increases.

Since the metric for each coordinate is identical and can be decomposed, i.e., $h_{ijkl} = \delta_{ik} \bar{h}_{jl}$, it is sufficient to analyze a $d \times d$ positive-definite matrix $\bar{H} := (\bar{h}_{ji})$ where

$$\bar{h}_{jl} = \int_0^T B_j(t) B_l(t) dt. \quad (9)$$

Let $\{\lambda_i\}$ be the eigenvalues of \bar{H} ; we consider $\frac{1}{d} \sum_{i=1}^d [(\log \lambda_i - \frac{1}{d} \sum_i \log \lambda_i)^2]$ as the measure of how far \bar{H} from being a scaled identity metric. Fig. 5 (Left) shows the variance of log eigenvalues as a function of d ; it is an increasing function, indicating \bar{H} becomes more non-isotropic as d increases. Fig. 5 (Right) shows the distribution of eigenvalues at $d = 15$. We note that 9 eigenvalues are located very close to zero, meaning that there is a 9-dimensional subspace $S \subset \mathbb{R}^{15}$, in which a vector $v \in S$ produces $v^T \bar{H} v \approx 0$. This means that changes in the control points within this subspace do not lead to significant changes in the motions $x(t; \theta)$; see Fig. 6 for an example.

On the other hand, we can discover d orthogonal direction vectors v_1, \dots, v_d by using eigenvectors of \bar{H} . Then, by dividing them by their Riemannian norms, i.e., $v_i \mapsto u_i = v_i / (v_i^T \bar{H} v_i)^{1/2}$, we can find d orthonormal vectors. Fig. 7 shows $x(t; \theta + \Delta\theta_i)$ for $i = 1, \dots, d$ where $\Delta\theta_i = (u_i^T; u_i^T) \in \mathbb{R}^{2 \times 10}$. We note that the degrees of changes in motions induced by 10 different displacement vectors $\Delta\theta_i$ are similar to each other unlike the case in Fig. 6. Therefore, we can conclude that taking into account the CurveGeom metric in the curve parameter space Θ is very important, to capture the geometry of the motion space.

IV. ISOMETRIC MOTION MANIFOLD PRIMITIVES

In this section, we propose an algorithm for learning isometric motion manifold primitives, adopting the general framework for isometric regularization from [29] and using the proposed CurveGeom Riemannian metric. Throughout, we adopt the autoencoder-based manifold learning framework [5] and denote an encoder by $g : \Theta \rightarrow \mathcal{Z}$ and a decoder by

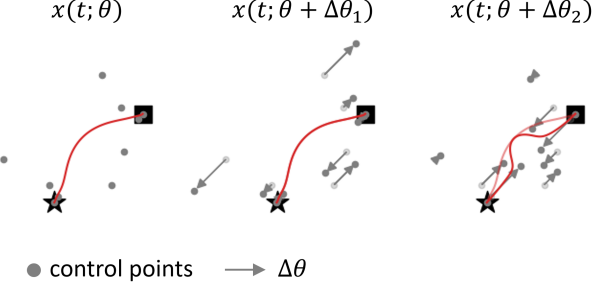


Fig. 6. Although the displacement vectors $\Delta\theta_1$ and $\Delta\theta_2$ have the same Euclidean norms, i.e., $\|\Delta\theta_1\| = \|\Delta\theta_2\|$, the degrees of changes in motions are significantly different: $\int \|x(t; \theta + \Delta\theta_2) - x(t; \theta)\| dt \gg \int \|x(t; \theta + \Delta\theta_1) - x(t; \theta)\| dt$.

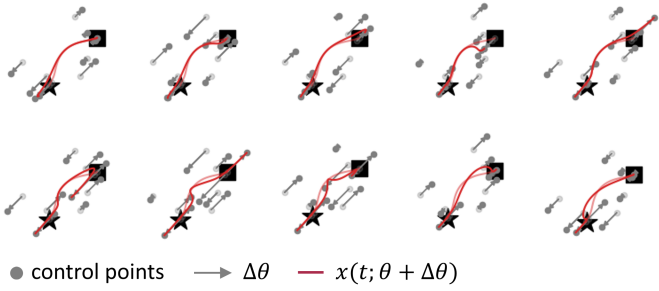


Fig. 7. For the CurveGeom metric H at $d = 10$, given $x(t; \theta)$ shown in Fig. 6, visualizations of $\{x(t; \theta + \Delta\theta_i)\}_{i=1}^{10}$ with 10 orthonormal direction displacement vectors $\{\Delta\theta_i\}$.

$f : \mathcal{Z} \rightarrow \Theta$. For simplicity, we will restrict our attention to the linear curve cases and denote by $\theta \in \Theta = \mathbb{R}^{n \times d}$ and $z \in \mathcal{Z} = \mathbb{R}^m$. We define $f^i : \mathcal{Z} \rightarrow \mathbb{R}^d$ that outputs the i -th component of $f(z)$, so that $f(z) = (f^1(z)^T; \dots; f^n(z)^T)$. Further, we denote by $J_{f^i}(z) = \frac{\partial f^i(z)}{\partial z} \in \mathbb{R}^{d \times m}$ and $\bar{H} = (\bar{h}_{jl})$ – which is a constant $d \times d$ positive-definite matrix – where $h_{ijkl} = \delta_{ik}\bar{h}_{jl}$.

The isometric regularization attempts to find a scaled isometric decoder f which preserves the geometric structure between \mathcal{Z} and Θ . Suppose the geometry of these spaces is specified with the Euclidean metric for \mathcal{Z} and CurveGeom Riemannian metric $h_{ijkl} = \delta_{ik}\bar{h}_{jl}$ for Θ , then a mapping f is a scaled isometry if it preserves inner products between the two spaces up to a scalar multiplication:

Proposition 3. *The decoder f is a scaled isometry if, for some positive scalar $c > 0$,*

$$I = c J_{f^i}(z)^T \bar{H} J_{f^i}(z) \quad (10)$$

for all $z \in \mathcal{Z}$ and all $i = 1, \dots, n$.

Proof. Rewriting (10), we can recover the original scaled isometry condition in [29]: $\delta_{ab} = c \sum_{j,l} \bar{h}_{jl} \frac{\partial f^{ij}}{\partial z^a} \frac{\partial f^{il}}{\partial z^b} = c \sum_{j,k,l} \delta_{ik} \bar{h}_{jl} \frac{\partial f^{ij}}{\partial z^a} \frac{\partial f^{kl}}{\partial z^b} = c \sum_{j,k,l} h_{ijkl} \frac{\partial f^{ij}}{\partial z^a} \frac{\partial f^{kl}}{\partial z^b}$ for all i , which implies $\delta_{ab} = \frac{c}{n} \sum_{i,j,k,l} h_{ijkl} \frac{\partial f^{ij}}{\partial z^a} \frac{\partial f^{kl}}{\partial z^b}$. \square

Let $\{\lambda_{ia}(z)\}_{a=1}^m$ be the eigenvalues of $J_{f^i}(z)^T \bar{H} J_{f^i}(z)$, then the condition (10) is equivalent to $\lambda_{ia}(z) = c$ for some positive scalar $c > 0$ and for all z, i and a . With a slight modification from [29], a coordinate-invariant relaxed

distortion measure that is a functional of f which measures how close f from being a scaled isometry (in the support of a probability density $p_{\mathcal{Z}}$ in \mathcal{Z}) can be defined as follows:

$$\begin{aligned} \mathcal{F}(f) &:= \mathbb{E}_{z \sim p_{\mathcal{Z}}} \left[\sum_{i,a} \left(\frac{\lambda_{ia}}{\mathbb{E}_{z \sim p_{\mathcal{Z}}} [\sum_{i,a} \lambda_{ia} / nm]} - 1 \right)^2 \right] \\ &= (nm)^2 \frac{\mathbb{E}_{z \sim p_{\mathcal{Z}}} [\sum_i \text{Tr}((J_{f^i}^T \bar{H} J_{f^i})^2)]}{\mathbb{E}_{z \sim p_{\mathcal{Z}}} [\sum_i \text{Tr}(J_{f^i}^T \bar{H} J_{f^i})]^2} - nm, \end{aligned} \quad (11)$$

which is minimal if and only if f is any scaled isometry (to see why, consider when $\lambda_{ia} = c$).

Let $\{\theta_i \in \Theta\}_{i=1}^N$ be a set of curve parameters that fit demonstration trajectories. The loss function that a pair of mappings, an encoder f and a decoder g , minimizes is

$$\frac{1}{N} \sum_{i=1}^N \|\theta_i - f \circ g(\theta_i)\|^2 + \alpha \frac{\mathbb{E}_{z \sim p_{\mathcal{Z}}} [\sum_i \text{Tr}((J_{f^i}^T \bar{H} J_{f^i})^2)]}{\mathbb{E}_{z \sim p_{\mathcal{Z}}} [\sum_i \text{Tr}(J_{f^i}^T \bar{H} J_{f^i})]^2}, \quad (12)$$

where α is a regularization coefficient and $p_{\mathcal{Z}}$ is set to be an empirical encoded data distribution $p_{\mathcal{Z}} := \frac{1}{N} \sum_{i=1}^N \delta(z - g(\theta_i))$. Once f and g are trained, we fit a density function, e.g., a Gaussian mixture model, with $\{g(\theta_i)\}_{i=1}^N$. We consider the trained decoder f and the density model in \mathcal{Z} as the **Isometric Motion Manifold Primitives (IMMP)**.

In practice, instead of computing the entire Jacobian J_{f^i} which is computation-heavy, we use the Hutchinson stochastic trace estimator, i.e., $\text{Tr}(A) = \mathbb{E}_{v \sim \mathcal{N}(0, I)} [v^T A v]$, so that the relaxed distortion measure can be approximated without the full Jacobian computation. Specifically, the regularization term can be computed as follows:

$$\frac{\mathbb{E}_{z \sim p_{\mathcal{Z}}} [\sum_i \mathbb{E}_{v \sim \mathcal{N}(0, I)} [v^T (J_{f^i}^T \bar{H} J_{f^i})^2 v]]}{\mathbb{E}_{z \sim p_{\mathcal{Z}}} [\sum_i \mathbb{E}_{v \sim \mathcal{N}(0, I)} [v^T J_{f^i}^T \bar{H} J_{f^i} v]]^2}. \quad (13)$$

We use one random sample v at each iteration of the gradient descent, and the $J_{f^i} \cdot v$ and $(\bar{H} J_{f^i} v)^T \cdot J_{f^i}$ can be efficiently computed by using the Jacobian-vector and vector-Jacobian products, respectively. Additionally, to expand the influence of the regularization effects to regions in between data, we use an augmented latent distribution for $p_{\mathcal{Z}}$. Sampling from the augmented $p_{\mathcal{Z}}$ is done by $\delta z_i + (1 - \delta)z_j$ where δ is uniformly sampled from $[-\eta, 1 + \eta]$ (we set $\eta = 0.2$ throughout) and $z_i = g(\theta_i)$ and $z_j = g(\theta_j)$ with $\theta_i, \theta_j \sim \{\theta_i\}_{i=1}^N$. Fig. 8 shows an IMMP result compared to the vanilla MMP with the example in Fig. 3 in the Introduction section.

A. IMM π : Isometric Motion Manifold Policy

In this section, we introduce how to construct a feedback policy, by adopting the IMMP framework. Let \mathcal{S} be a state space. Suppose we are given a set of state-trajectories pairs data, i.e., $\{(s_i, x_i^j)\}_i$ where multiple demonstration trajectories $\{x_i^j\}_j$ are given for each state s_i . First, we fit the curve parameter $\theta_i^j \in \Theta$ for each x_i^j . Second, we train a conditional autoencoder as done in [2], where an encoder $g : \Theta \rightarrow \mathcal{Z}$ and decoder $f : \mathcal{Z} \times \mathcal{S} \rightarrow \Theta$. In this step, we apply the isometric regularization at each s_i for the mapping $f(\cdot, s_i) : \mathcal{Z} \rightarrow \Theta$. Third, we fit a Gaussian mixture model for each s_i by using $\{g(\theta_i^j)\}_j$, obtaining $\{(\mu_i^k, \Sigma_i^k)\}_k$ (k denotes

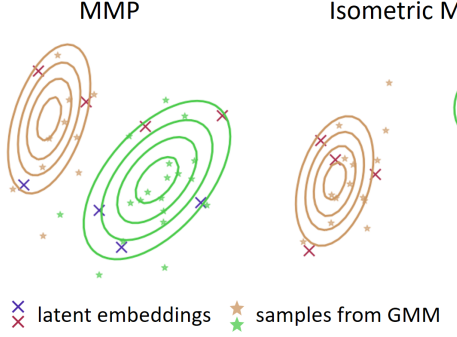


Fig. 8. MMP and IMMP: Two-dimensional latent space representations of the trajectories shown in Fig. 3 and the GMM fitting results.

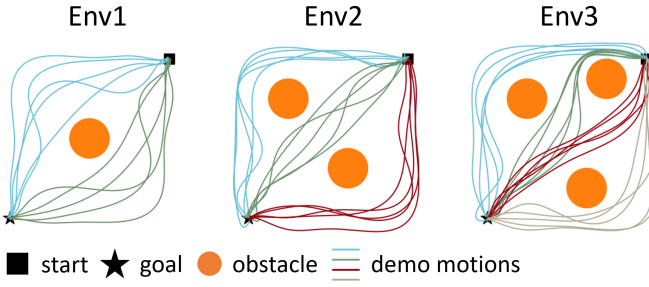


Fig. 9. Three environments where training demonstration trajectories are fitted with the Bezier curves of degree 9.

the mixture component). Lastly, we fit a neural network GMM estimator that maps $s \in \mathcal{S} \mapsto \{(\mu^k(s), \Sigma^k(s))\}_k$, by using the dataset $\{s_i, \{(\mu_i^k, \Sigma_i^k)\}_k\}_i$ and minimizing optimal transport distance between GMMs. Consequently, we obtain a stochastic feedback policy that maps a state to the GMM parameters where we can sample desired trajectories, which we call the **Isometric Motion Manifold Policy (IMM π)**.

V. EXPERIMENTS

In this section, we conduct manifold primitive and policy learning experiments: (i) two-dimensional obstacle-avoiding motion generation tasks and (ii) pushing manipulation tasks via feedback policies. Throughout, we use the Bezier curve model for $x(t; \theta)$, and compare the vanilla autoencoder – which we denote by *MMP* –, the autoencoder with isometric regularization using the identity metric – which we denote by *IMMP (Identity)* [29] –, and the autoencoder with isometric regularization using the proposed CurveGeom Riemannian metric – which we denote by *IMMP (CurveGeom)*. We use Gaussian mixture models to fit $p_Z(z)$ given encoded data by trained encoders.

A. Planar Obstacle-Avoiding Motions

We consider three different environments with different numbers of obstacles and obstacle-avoiding trajectories; see Env1, Env2, and Env3 in Fig. 9. The number of total training trajectories for each environment setting is 10, 15, and 20, respectively. These trajectories can be grouped based on the homotopy type; there are two, three, and four groups of

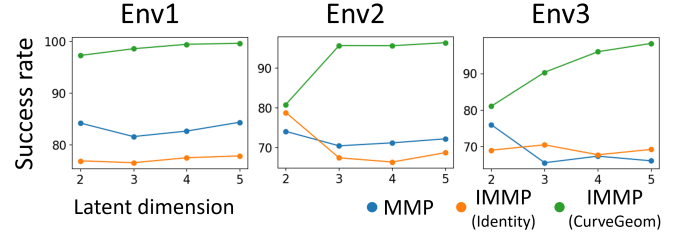


Fig. 10. Success rates as functions of the autoencoder latent space dimensions.

TABLE I

AVERAGES AND STANDARD ERRORS OF THE SUCCESS RATES OF THE MMP AND IMMPs WITH 5 TIMES RUN WITH DIFFERENT RANDOM SEEDS; THE HIGHER THE BETTER. THE BEST RESULTS ARE MARKED IN BOLD.

	Env1	Env2	Env3
MMP	84.34 ± 4.15	74.02 ± 0.96	75.96 ± 2.33
IMMP (Identity)	77.82 ± 0.89	78.78 ± 0.21	70.46 ± 1.72
IMMP (CurveGeom)	99.62 ± 0.16	95.66 ± 1.44	98.22 ± 0.35

homotopic trajectories for each environment, respectively. We train MMP, IMMP (Identity), and IMMP (CurveGeom) and fit Gaussian mixture models that have two, three, and four components for each environment, respectively.

The number of control points is desired to be as small as possible to reduce the dimension of Θ ; it is set to be 10 thus Θ is 20-dimensional. The encoder and decoder are 4-layer fully connected neural networks with 256 nodes and ELU activation functions. We add a projection layer at the end of the decoder so that the initial and terminal control points coincide with the start and goal positions. When sampling latent points from the GMM, we reject the samples with likelihood values lower than the threshold value η – where η is set to be the minimum value among the likelihood values of the training trajectories. A generated trajectory is considered successful if it does not collide with the obstacles.

We train MMP and IMMP models with 2, 3, 4, and 5-dimensional latent spaces with five different random seeds. For IMMPs, the regularization coefficient α is searched over 0.01, 0.1, and 1. Fig. 10 shows the success rates as functions of the latent space dimensions – which are measured with 1000 generated trajectories – and the best results are shown in Table I. The IMMPs trained with the CurveGeom metrics show significantly higher success rates than the others.

Fig. 10 shows that the success rate of our IMMP (CurveGeom) increases as the latent space dimension increases, while those of other methods either oscillate or decrease. While the success rate of our IMMP is already high with the two-dimensional latent space for the Env1 setting, the minimum latent space dimension required to show a good performance becomes higher for more complex settings Env2 and Env3. Fig. 11 shows some generated trajectories, demonstrating that only the IMMPs with the CurveGeom metrics have learned the correct clustering structures of homotopy.

B. Robotic Pushing Manipulation Tasks

In this section, we compare MM π and our IMM π with pushing manipulation tasks, where the goal is to push a cube to

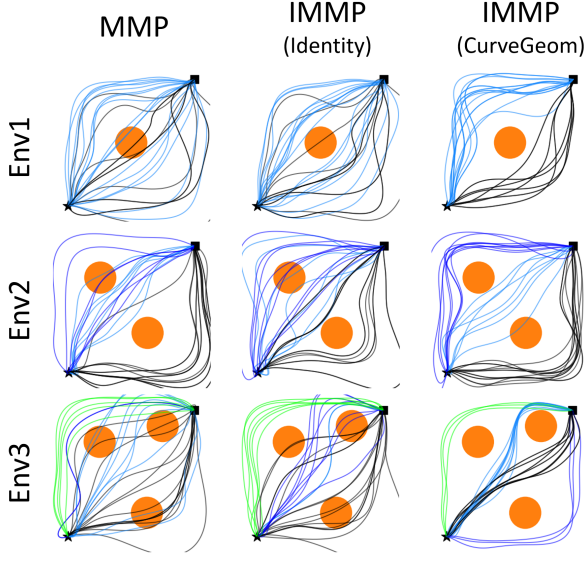


Fig. 11. Trajectories generated by trained MMP and IMMPs, where we first obtain latent samples from GMM and then decode them; the GMM component numbers are 2, 3, and 4 for Env1, Env2, and Env3, respectively (samples from the same GMM component are assigned the same color).

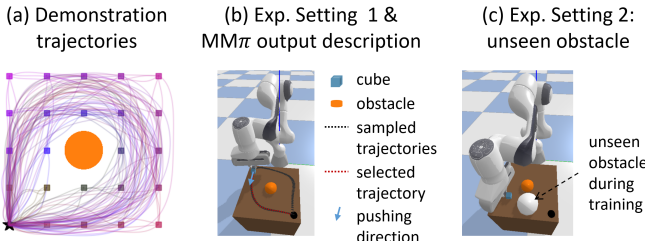


Fig. 12. (a) A set of state-trajectories pairs data. (b) The pushing direction is determined from the $MM\pi$ output trajectory. (c) An unseen obstacle suddenly appears and the robot needs to adapt.

the goal position without colliding with obstacles (see Fig. 12 (b)). We may use the motion manifold primitives trained in the previous section, plan a desired trajectory for the cube, and perform a PID feedback tracking control. However, this approach is limited in adapting to an unexpected situation where the previously planned trajectory becomes infeasible (e.g., an unseen obstacle appears that blocks the planned trajectory; see Fig. 12 (c)). It is more powerful, although it requires more data, to train a feedback policy that can generate a manifold of motions given for each state.

In this example, the state is given as the current xy position of the cube and the action is defined as the xy pushing direction. The motion manifold policies are trained with a set of state-trajectories pairs data shown in Fig. 12 (a), where we select the latent space dimension to be 5 and the number of mixture components to be 2 in GMM (other details such as network architectures are similar to those described in the previous section). Given multiple sampled trajectories from the policy output, we select the one that is optimal – for this problem, we consider the shortest length curve as being optimal – and satisfies additional task constraints (e.g., avoiding unseen obstacles); we then use the initial velocity direction as the pushing direction (see Fig. 12 (b)).

TABLE II
THE SUCCESS RATES OF THE $MM\pi$ AND $IMM\pi$ s WITH 25 INITIAL STATES; THE HIGHER THE BETTER. IN EXP. SETTING 2, A NEW UNSEEN OBSTACLE APPEARS THAT BLOCKS THE PASSAGE IN WHICH THE SHORTEST PATH EXISTS. THE BEST RESULTS ARE MARKED IN BOLD.

	$MM\pi$	$IMM\pi$ (Identity)	$IMM\pi$ (CurveGeom)
Exp. 1	11/25	1/25	25/25
Exp. 2	0/25	0/25	25/25

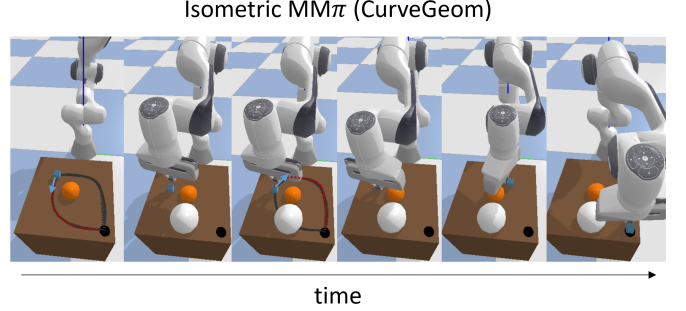


Fig. 13. $IMM\pi$ first opts for a route that passes beneath the orange obstacle. When a new obstacle emerges and obstructs this route (in the second figure), it can then choose an alternative path that avoids collisions by going above the orange obstacle.

We consider two experiment settings (see Fig. 12 (b) and (c)), where, in setting 1, the robot is required to push the cube without colliding with the orange obstacle shown in training. In setting 2, after a robot pushes the cube two times, a new unseen obstacle suddenly appears that blocks the passage where the shortest path exists; thus the robot needs to push the cube toward the other passage to avoid collisions. All the experiments are conducted in the PyBullet simulation.

We run the experiments with 25 different initial cube states and report the success rates in Table II. If the cube is moved to the target location without colliding with any obstacle within 50 pushes, it is considered successful. As shown in the table, our $IMM\pi$ s trained with CurveGeom metrics only show successful results. Fig. 13 illustrates how our $IMM\pi$ successfully adapts when a new unseen obstacle appears.

VI. CONCLUSION

We have constructed a CurveGeom Riemannian metric for the parametric curve space and proposed the isometric regularization for the motion manifold primitives – where the geometry of the motion manifold is preserved in the latent space –, leading to a significantly enhanced latent space density fitting result. We have shown that, while the vanilla MMP severely fails in generating collision-free motions, the IMMP and $IMM\pi$ are able to produce correct motions. One drawback of $IMM\pi$ is that it requires a lot of demonstration data (i.e., multiple trajectories for each state), limiting its scalability. We believe that a combination of supervised learning from demonstration and reinforcement learning framework holds the potential to develop a scalable training method for the $IMM\pi$, pointing towards a promising future direction.

ACKNOWLEDGMENTS

Yonghyeon Lee was the beneficiary of an individual grant from CAINS supported by a KIAS Individual Grant

(AP092701) via the Center for AI and Natural Sciences at Korea Institute for Advanced Study.

REFERENCES

- [1] M. Noseworthy, R. Paul, S. Roy, D. Park, and N. Roy, “Task-conditioned variational autoencoders for learning movement primitives,” in *Conference on robot learning*. PMLR, 2020, pp. 933–944.
- [2] B. Lee, Y. Lee, S. Kim, M. Son, and F. C. Park, “Equivariant motion manifold primitives,” in *7th Annual Conference on Robot Learning*, 2023.
- [3] J. B. Tenenbaum, V. d. Silva, and J. C. Langford, “A global geometric framework for nonlinear dimensionality reduction,” *science*, vol. 290, no. 5500, pp. 2319–2323, 2000.
- [4] Y. Bengio, A. Courville, and P. Vincent, “Representation learning: A review and new perspectives,” *IEEE transactions on pattern analysis and machine intelligence*, vol. 35, no. 8, pp. 1798–1828, 2013.
- [5] Y. Lee, “A geometric perspective on autoencoders,” *arXiv preprint arXiv:2309.08247*, 2023.
- [6] A. J. Ijspeert, J. Nakanishi, H. Hoffmann, P. Pastor, and S. Schaal, “Dynamical movement primitives: learning attractor models for motor behaviors,” *Neural computation*, vol. 25, no. 2, pp. 328–373, 2013.
- [7] S. Schaal, P. Mohajerian, and A. Ijspeert, “Dynamics systems vs. optimal control—a unifying view,” *Progress in brain research*, vol. 165, pp. 425–445, 2007.
- [8] A. Pervez, A. Ali, J.-H. Ryu, and D. Lee, “Novel learning from demonstration approach for repetitive teleoperation tasks,” in *2017 IEEE World Haptics Conference (WHC)*. IEEE, 2017, pp. 60–65.
- [9] Y. Fanger, J. Umlauft, and S. Hirche, “Gaussian processes for dynamic movement primitives with application in knowledge-based cooperation,” in *2016 IEEE/RSJ International Conference on Intelligent Robots and Systems (IROS)*. IEEE, 2016, pp. 3913–3919.
- [10] J. Umlauft, Y. Fanger, and S. Hirche, “Bayesian uncertainty modeling for programming by demonstration,” in *2017 IEEE International Conference on Robotics and Automation (ICRA)*. IEEE, 2017, pp. 6428–6434.
- [11] A. Pervez, Y. Mao, and D. Lee, “Learning deep movement primitives using convolutional neural networks,” in *2017 IEEE-RAS 17th international conference on humanoid robotics (Humanoids)*. IEEE, 2017, pp. 191–197.
- [12] S. M. Khansari-Zadeh and A. Billard, “Learning stable nonlinear dynamical systems with gaussian mixture models,” *IEEE Transactions on Robotics*, vol. 27, no. 5, pp. 943–957, 2011.
- [13] K. Neumann, A. Lemme, and J. J. Steil, “Neural learning of stable dynamical systems based on data-driven lyapunov candidates,” in *2013 IEEE/RSJ International Conference on Intelligent Robots and Systems*. IEEE, 2013, pp. 1216–1222.
- [14] K. Neumann and J. J. Steil, “Learning robot motions with stable dynamical systems under diffeomorphic transformations,” *Robotics and Autonomous Systems*, vol. 70, pp. 1–15, 2015.
- [15] C. Blocher, M. Saveriano, and D. Lee, “Learning stable dynamical systems using contraction theory,” in *2017 14th International Conference on Ubiquitous Robots and Ambient Intelligence (URAI)*. IEEE, 2017, pp. 124–129.
- [16] V. Sindhwan, S. Tu, and M. Khansari, “Learning contracting vector fields for stable imitation learning,” *arXiv preprint arXiv:1804.04878*, 2018.
- [17] J. Z. Kolter and G. Manek, “Learning stable deep dynamics models,” *Advances in neural information processing systems*, vol. 32, 2019.
- [18] G. Maeda, M. Ewerton, T. Osa, B. Busch, and J. Peters, “Active incremental learning of robot movement primitives,” in *Conference on Robot Learning*. PMLR, 2017, pp. 37–46.
- [19] N. Jaquier, D. Ginsbourger, and S. Calinon, “Learning from demonstration with model-based gaussian process,” in *Conference on Robot Learning*. PMLR, 2020, pp. 247–257.
- [20] S. Calinon, “A tutorial on task-parameterized movement learning and retrieval,” *Intelligent service robotics*, vol. 9, pp. 1–29, 2016.
- [21] D. A. Duque, F. A. Prieto, and J. G. Hoyos, “Trajectory generation for robotic assembly operations using learning by demonstration,” *Robotics and Computer-Integrated Manufacturing*, vol. 57, pp. 292–302, 2019.
- [22] C. Yang, C. Chen, N. Wang, Z. Ju, J. Fu, and M. Wang, “Biologically inspired motion modeling and neural control for robot learning from demonstrations,” *IEEE Transactions on Cognitive and Developmental Systems*, vol. 11, no. 2, pp. 281–291, 2018.
- [23] A. Paraschos, C. Daniel, J. R. Peters, and G. Neumann, “Probabilistic movement primitives,” *Advances in neural information processing systems*, vol. 26, 2013.
- [24] Y. Huang, L. Rozo, J. Silvério, and D. G. Caldwell, “Kernelized movement primitives,” *The International Journal of Robotics Research*, vol. 38, no. 7, pp. 833–852, 2019.
- [25] T. Osa, A. M. G. Esfahani, R. Stolkin, R. Lioutikov, J. Peters, and G. Neumann, “Guiding trajectory optimization by demonstrated distributions,” *IEEE Robotics and Automation Letters*, vol. 2, no. 2, pp. 819–826, 2017.
- [26] P. Bézier, “Essai de définition numérique des courbes et des surfaces expérimentales: contribution à l'étude des propriétés des courbes et des surfaces paramétriques polynomiales à coefficients vectoriels,” Ph.D. dissertation, these de Doctoral d'Etat es Sciences Physiques, 1977.
- [27] Y. Lee, H. Kwon, and F. Park, “Neighborhood reconstructing autoencoders,” *Advances in Neural Information Processing Systems*, vol. 34, pp. 536–546, 2021.
- [28] Y. Lee, S. Kim, J. Choi, and F. Park, “A statistical manifold framework for point cloud data,” in *International Conference on Machine Learning*. PMLR, 2022, pp. 12378–12402.
- [29] Y. Lee, S. Yoon, M. Son, and F. C. Park, “Regularized autoencoders for isometric representation learning,” in *International Conference on Learning Representations*, 2022.
- [30] C. Jang, Y. Lee, Y.-K. Noh, and F. C. Park, “Geometrically regularized autoencoders for non-euclidean data,” in *The Eleventh International Conference on Learning Representations*.
- [31] Y. Lee and F. C. Park, “On explicit curvature regularization in deep generative models,” *arXiv preprint arXiv:2309.10237*, 2023.
- [32] D. P. Kingma and M. Welling, “Auto-encoding variational bayes,” *arXiv preprint arXiv:1312.6114*, 2013.
- [33] A. Creswell, Y. Mohamed, B. Sengupta, and A. A. Bharath, “Adversarial information factorization,” *arXiv preprint arXiv:1711.05175*, 2017.
- [34] S. Rifai, P. Vincent, X. Muller, X. Glorot, and Y. Bengio, “Contractive auto-encoders: Explicit invariance during feature extraction,” in *Proceedings of the 28th international conference on international conference on machine learning*, 2011, pp. 833–840.
- [35] P. Nazari, S. Damrich, and F. A. Hamprecht, “Geometric autoencoders—what you see is what you decode,” 2023.
- [36] S. Yoon, Y.-K. Noh, and F. Park, “Autoencoding under normalization constraints,” in *International Conference on Machine Learning*. PMLR, 2021, pp. 12087–12097.
- [37] H. Shao, A. Kumar, and P. Thomas Fletcher, “The riemannian geometry of deep generative models,” in *Proceedings of the IEEE Conference on Computer Vision and Pattern Recognition Workshops*, 2018, pp. 315–323.
- [38] G. Arvanitidis, L. K. Hansen, and S. Hauberg, “Latent space oddity: on the curvature of deep generative models,” *arXiv preprint arXiv:1710.11379*, 2017.
- [39] F. C. Park, “Distance metrics on the rigid-body motions with applications to mechanism design,” 1995.
- [40] S. Said, N. Court, N. Le Bihan, and S. J. Sangwine, “Exact principal geodesic analysis for data on so (3),” in *2007 15th European Signal Processing Conference*. IEEE, 2007, pp. 1701–1705.
- [41] X. Pennec, P. Fillard, and N. Ayache, “A riemannian framework for tensor computing,” *International Journal of computer vision*, vol. 66, pp. 41–66, 2006.
- [42] V. Arsigny, P. Fillard, X. Pennec, and N. Ayache, “Log-euclidean metrics for fast and simple calculus on diffusion tensors,” *Magnetic Resonance in Medicine: An Official Journal of the International Society for Magnetic Resonance in Medicine*, vol. 56, no. 2, pp. 411–421, 2006.
- [43] T. Lee and F. C. Park, “A geometric algorithm for robust multibody inertial parameter identification,” *IEEE Robotics and Automation Letters*, vol. 3, no. 3, pp. 2455–2462, 2018.
- [44] T. Shnitzer, M. Yurochkin, K. Greenewald, and J. M. Solomon, “Log-euclidean signatures for intrinsic distances between unaligned datasets,” in *International Conference on Machine Learning*. PMLR, 2022, pp. 20106–20124.
- [45] T. Bendokat, R. Zimmermann, and P.-A. Absil, “A grassmann manifold handbook: Basic geometry and computational aspects,” *arXiv preprint arXiv:2011.13699*, 2020.
- [46] S.-i. Amari and H. Nagaoka, *Methods of information geometry*. American Mathematical Soc., 2000, vol. 191.
- [47] S.-i. Amari, *Information geometry and its applications*. Springer, 2016, vol. 194.
- [48] M. Han and F. C. Park, “Dti segmentation and fiber tracking using metrics on multivariate normal distributions,” *Journal of mathematical imaging and vision*, vol. 49, pp. 317–334, 2014.